Chinese Chemical Letters 36 (2025) 111059

Contents lists available at ScienceDirect

Chinese Chemical Letters

journal homepage: www.elsevier.com/locate/cclet

Ultrasmall PtCu nanosheets as a broadband phototheranostic agent in near-infrared biowindow

Ying Zhang[a], Chuang Shen[a], Jiaxu Zhang[a], Qi Shen[a], Fei Xu[a], Shengheng Wang[a], Jiuyi Hu[b], Faisal Saleem[b,*], Feng Huang[c,*], Zhimin Luo[a,*]

[a] State Key Laboratory of Flexible Electronics (LoFE) & Jiangsu Key Laboratory of Smart Biomaterials and Theranostic Technology, Institute of Advanced Materials (IAM), College of Electronic and Optical Engineering & College of Flexible Electronics (Future Technology), School of Chemistry and Life Sciences, Nanjing University of Posts and Telecommunications, Nanjing 210023, China
[b] State Key Laboratory of Flexible Electronics (LoFE) & Institute of Advanced Materials (IAM), School of Flexible Electronics (Future Technologies), Nanjing Tech University (NanjingTech), Nanjing 211816, China
[c] Department of Human Anatomy, Laboratory of Clinical Applied Anatomy, Key Laboratory of Brain Aging and Neurodegenerative Diseases of Fujian Province, School of Basic Medical Sciences, Fujian Medical University, Fuzhou 350122, China

ARTICLE INFO

Article history:
Received 13 January 2025
Revised 4 March 2025
Accepted 7 March 2025
Available online 12 March 2025

Keywords:
Noble metal nanostructures
PtCu nanosheets
Photothermal therapy
Photoacoustic imaging
Broadband phototheranostics

ABSTRACT

Broadband photothermal and photoacoustic agents in the near-infrared (NIR) biowindow are of significance for cancer phototheranostics. In this work, PtCu nanosheets with an average lateral size of less than 10 nm are synthesized as NIR photothermal and photoacoustic agents *in vivo*, which show strong light absorption from NIR-I to NIR-II biowindows with the photothermal conversion efficiencies of 20.4% under 808 nm laser and 32.7% under 1064 nm laser. PtCu nanosheets functionalized with folic acid-modified thiol-poly(ethylene glycol) (SH-PEG-FA) present good biocompatibility and 4T1 tumor-targeted effect, which give high-contrast photoacoustic imaging and efficient photothermal ablation of 4T1 tumor in both NIR-I and NIR-II biowindows. Our work significantly broadens applications of noble metal-based nanomaterials in the fields of cancer phototheranostics by rationally designing their structures and modulating their physicochemical properties.

Photothermal therapy (PTT) and photoacoustic imaging (PAI) are becoming useful technologies for cancer phototheranostics [1]. PTT has received widespread attention due to its high controllability, noninvasiveness and low adverse side effects in the treatment of tumors [2,3]. PAI, a promising biomedical molecular imaging technique, has attracted great interest due to its high imaging contrast and resolution, low scattering and dissipation in biological tissues, and excellent biological tissue permeability [4]. To date, many multifunctional inorganic nanomaterials have been prepared for PAI and PTT, such as carbon nanomaterials [5–9], transition metal chalcogenides [10–16], noble metal nanostructures [17–25], transition metal oxides [26,27], and metal-organic framework [28,29]. Noble metal nanostructures (Au nanorods [17,19,21,25], Au nanocages [23,30], Au nanoshells [31], Au nanovesicles [20,32], AuAg nanoalloy [33], and so on) have attracted great attention for phototherapeutics because of their prominent ability to absorb near-infrared (NIR) light and convert it into thermal energy. However, most of photothermal and photoacoustic agents based on noble metal nanostructures fall in the first NIR biowindow (NIR-I, 750–1000 nm). The efficacy of NIR-I PTT and PAI *in vivo* is often limited by the relatively small maximum permissible exposure and short penetration depth of NIR-I laser. Promisingly, it is found that the lasers in the second NIR biowindow (NIR-II, 1000–1350 nm) have larger penetration depth and maximum permissible exposure as compared to NIR-I lasers for phototherapeutics *in vivo*. Great effort has been made to develop noble metal nanostructures with strong absorption in the NIR-II biowindow as photothermal and photoacoustic agents in recent years. However, few noble metal nanostructures can meet the requirements of PTT and PAI *in vivo* due to their large sizes or low photothermal conversion efficiency (PCE). Therefore, development of ultrasmall and unique noble metal nanostructures with strong broadband NIR photothermal and photoacoustic properties is eagerly expected for phototherapeutics *in vivo*.

Two-dimensional (2D) noble metal nanostructures are considered to be potential NIR photothermal and photoacoustic agents due to their fascinating optical properties derived from special 2D structures [18,24,34–36]. Regulating the shape of noble metal

* Corresponding authors.
E-mail addresses: iamfaisalsaleem@njtech.edu.cn (F. Saleem), huangfeng@fjmu.edu.cn (F. Huang), iamzmluo@njupt.edu.cn (Z. Luo).

https://doi.org/10.1016/j.cclet.2025.111059
1001-8417/

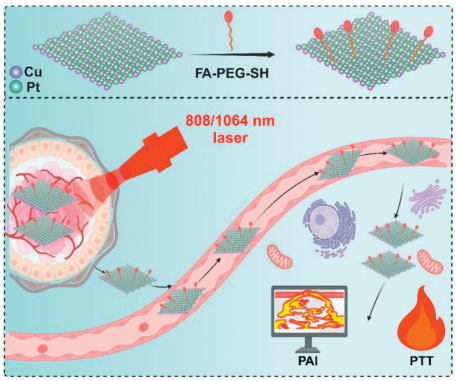

Scheme 1. SH-PEG-FA functionalized PtCu nanosheets for 4T1 tumor-targeted PTT and PAI in both NIR-I and NIR-II windows. SH-PEG-FA: folic acid-modified thiol-poly(ethylene glycol).

nanostructures to 2D morphology can extend their strong absorption wavelength to NIR-II window. For example, Ag nanoparticles have almost no absorption in NIR-II window, while Ag nanoplates display evident NIR-II light adsorption [34]. Ultrathin Pd nanosheets give much stronger absorbance in NIR-II window than Pd nanoparticles, which enhances their applications as photothermal and photoacoustic agents in broadband NIR windows [37]. Pt nanostructures with good biocompatibility display high-order longitudinal surface plasmon resonance (SPR) mode in NIR zone. Their SPR wavelengths can be elongated to NIR-II zone by adjusting their morphology and structures [38]. Therefore, it is theoretically feasible to construct 2D Pt-based alloy nanostructures as broadband NIR photothermal and photoacoustic agents.

In this work, alloyed strategy is developed to prepare 2D PtCu nanosheets with the lateral size of less than 10 nm. The ultrasmall PtCu nanosheets give broadband light absorption from NIR-I to NIR-II windows with the extinction coefficients of 7.11 L g^{-1} cm^{-1} at 808 nm and 2.06 L g^{-1} cm^{-1} at 1064 nm. The PCEs of PtCu nanosheets are 20.4% under 808 nm laser and 32.7% under 1064 nm laser. PtCu nanosheets exhibit strong photoacoustic effect under both 808 and 1064 nm lasers. PtCu nanosheets functionalized with folic acid-modified thiol-poly(ethylene glycol) (SH-PEG-FA) display good biocompatibility and 4T1 tumor-targeting function, which present high-contrast PAI and highly efficient photothermal ablation of 4T1 tumor in both NIR-I and NIR-II windows (Scheme 1). This kind of Pt-based alloy nanosheets enriches the family of advanced photothermal and photoacoustic agents.

PtCu nanosheets prepared by a modified two-step solvothermal method were characterized by transmission electron microscopy (TEM), high-resolution TEM (HRTEM), energy dispersive spectrometer (EDS) and X-ray photoelectron spectroscopy (XPS). As shown in Fig. 1a and Fig. S1 (Supporting information), our obtained PtCu

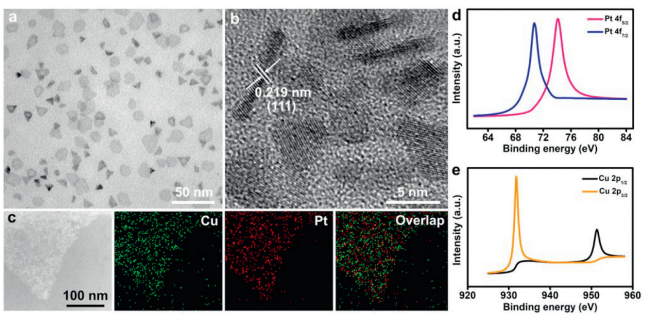

Fig. 1. (a) TEM, (b) HRTEM and (c) EDS elemental mapping images of PtCu nanosheets. High-resolution XPS spectra of (d) Pt 4f and (e) Cu 2p in PtCu nanosheets.

nanosheets have homogeneous size distribution with the average size of ~8 nm. HRTEM images in Fig. 1b show the crystalline fringes with the interplanar spacing of 0.219 nm corresponding to (111) plane of PtCu nanostructures [39]. EDS elemental mapping images in Fig. 1c confirm the compositions of Pt and Cu in the product. Survey XPS spectrum of PtCu nanosheets demonstrates the binding energies of Pt 4f (~72.8 eV) and Cu 2p (~933.5 eV), confirming their compositions of Pt and Cu elements. High-resolution XPS spectrum of Pt 4f (Fig. 1d) shows the binding energies at 70.7 and 74.1 eV attributed to Pt $4f_{7/2}$ and Pt $4f_{5/2}$ of zero-valent Pt, respectively [40]. The two binding energies at 931.8 and 951.3 eV (Fig. 1e) are attributable to Cu $2p_{3/2}$ and Cu $2p_{1/2}$ of zero-valent Cu, respectively [40]. High-resolution XPS spectra of Pt 4f and Cu 2p indicate that there is no oxidation state in PtCu nanosheets, proving the formation of PtCu alloy nanosheets. The atomic molar ration of Pt and Cu elements in PtCu nanosheets is evaluated from XPS characterization to be 1.18:1 (Fig. S2 and Table S1 in Supporting information).

In order to investigate the possibility of PtCu nanosheets applied as phototherapeutic agents, the photothermal property of PtCu nanosheets was studied. As shown in Fig. S3a (Supporting information), PtCu nanosheets show broadband light absorption from 300 nm to 1200 nm. The extinction coefficient (ε) of PtCu nanosheets is estimated to be 7.11 L g^{-1} cm^{-1} at 808 nm (Fig. S3b in Supporting information), which is higher than that of graphene oxides (3.6 L g^{-1} cm^{-1}) [8], CuCo nanosheets (5.37 L g^{-1} cm^{-1}) [41], germanene quantum dots (5.333 L g^{-1} cm^{-1}) [42] or gold nanorods (3.9 L g^{-1} cm^{-1}) [43]. Moreover, the ε value of PtCu nanosheets at 1064 nm (2.06 L g^{-1} cm^{-1}) (Fig. S3c in Supporting information) is also higher than that of carbon nanochips (1.32 L g^{-1} cm^{-1}) [44].

The photothermal heating curves under 808 nm (Fig. 2a) and 1064 nm (Fig. 2b) show that the temperatures of PtCu nanosheets aqueous suspensions increase with their concentrations and are dependent on the power density of laser (Fig. S4 in Supporting information). The temperature of PtCu nanosheets aqueous suspension (50 μg/mL) can rapidly reach 70 °C after the irradiation of 808 nm laser (1.0 W/cm^2) for 5 min. Furthermore, the temperature of PtCu nanosheets aqueous suspension (200 μg/mL) is also able to rapidly rise to 49 °C after the irradiation of 1064 nm laser (1.5 W/cm^2) for 6.5 min. It is indicated that PtCu nanosheets have good photothermal effect in both NIR-I and NIR-II biowindows. The corresponding photothermal images of PtCu nanosheets with different concentrations are presented in Fig. S5 (Supporting information). PCEs (η) of PtCu nanosheets are calculated according to the photothermal heating and cooling curves of PtCu nanosheets (Figs. 2c and d), which are 20.4% at 808 nm (Fig. 2e) and 32.7% at 1064 nm (Fig. 2f). The PCE of PtCu nanosheets at 1064 nm is higher than that of gold nanorods (25.9%) [45], Fe_3O_4@CuS nanoparticles (19.2%) [46], Pt nanoparticles (23.0%) [47] or Pt nanocubes (32.3%) [38]. Measurements of photothermal stability (Figs. 2g and h) demonstrate that the heating capacity of PtCu nanosheets under both 808 nm and 1064 nm lasers shows no significant deterioration during five lasers on/off cycles, indicating that PtCu nanosheets can be as a durable photothermal agent for PTT of cancers.

Owing to their strong absorption and marked PCE in both NIR-I and NIR-II regions, the photoacoustic property of PtCu nanosheets was further evaluated. The output laser energies of photoacoustic machine are ~160 mJ/pulse for Ti:Saph (808 nm) and ~300 mJ/pulse for Nd:YAG (1064 nm), and other parameters of the used photoacoustic machine are shown at Table S2 (Supporting information). The measured photoacoustic signals and corresponding photoacoustic images of PtCu nanosheets aqueous suspensions upon exposure to 808 and 1064 nm lasers can be seen in Fig. 3. The photoacoustic signal of PtCu nanosheets aqueous suspensions is much stronger than that of deionized water, and shows a great linear re-

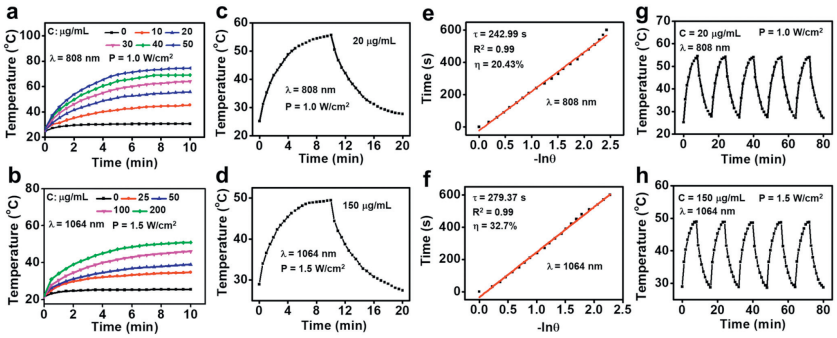

Fig. 2. Photothermal heating curves of PtCu nanosheets aqueous suspensions with varied concentrations under the irradiation of (a) 808 and (b) 1064 nm lasers. Photothermal heating and cooling curves of PtCu nanosheets aqueous suspensions through on/off (c) 808 and (d) 1064 nm lasers. Calculating the PCEs of PtCu nanosheets under (e) 808 and (f) 1064 nm lasers. Measuring photothermal stability of PtCu nanosheets through five (g) 808 or (h) 1064 nm laser on/off cycles.

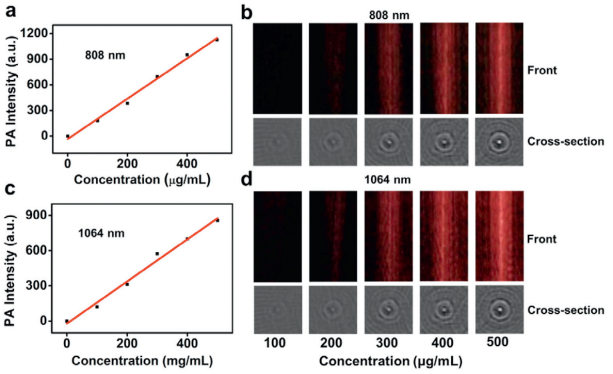

Fig. 3. (a) Photoacoustic signals of PtCu nanosheet aqueous suspensions (100, 200, 300, 400, 500 μg/mL) under 808 nm laser. (b) Photoacoustic images of PtCu nanosheet aqueous suspensions (100, 200, 300, 400, 500 μg/mL) in the front and cross section of photoacoustic tubes under 808 nm laser. (c) Photoacoustic signals of PtCu nanosheet aqueous suspensions (100, 200, 300, 400, 500 μg/mL) under 1064 nm laser. (d) Photoacoustic images of PtCu nanosheet aqueous suspensions (100, 200, 300, 400, 500 μg/mL) in the front and cross section of photoacoustic tubes under 1064 nm laser.

lationship with their concentrations under both 808 nm (Figs. 3a and b) and 1064 nm (Figs. 3c and d) lasers, indicating that PtCu nanosheets can be a prospective photoacoustic agent in both NIR-I and NIR-II biowindows.

Prior to PAI and PTT of PtCu nanosheets, HS-PEG-FA was used to modify PtCu nanosheets for improving their biocompatibility and endowing them with 4T1 tumor-targeting function. PtCu nanosheets modified with HS-PEG-FA (PtCu-PEG-FA) were characterized by TEM, ultraviolet-visible-near infrared (UV–vis-NIR) and XPS. As shown in Fig. S6 (Supporting information), the morphology and structure of PtCu nanosheets are not changed after functionalization with HS-PEG-FA. Fig. S7 (Supporting information) displays the absorption peak at 350 nm attributed to folic acid in HS-PEG-FA [48]. High-resolution S2p XPS spectrum (Fig. S8 in Supporting information) shows the binding energies at 162.3 and 163.2 eV, which can be ascribed to S $2p_{3/2}$ and S $2p_{1/2}$ of S-Pt and S-Cu bonds [49,50]. Results of photothermal measurements (Fig. S9 in Supporting information) show that the photothermal performance of PtCu nanosheets is not changed after modification with HS-PEG-FA. TEM, UV–vis-NIR and XPS characterizations were carried out to evaluate the photostability of PtCu-PEG-FA nanosheets. As shown in Figs. S10–S12 (Supporting information), the morphology, absorbance and composition of PtCu-PEG-FA nanosheets are not changed after laser irradiation, confirming the good stability of PtCu-PEG-FA nanosheets under irradiation with NIR laser. Biocompatibility of PtCu-PEG-FA nanosheets was evaluated by traditional tetrazolium-based colorimetric assay (MTT) using 4T1 cells as models. As shown in Fig. S13a (Supporting information), the cell viability is still over 90% for 4T1 cells incubated with PtCu-PEG-FA nanosheets (100 μg/mL) for 24 h without laser irradiation, indicating the low biological toxicity of PtCu-PEG-FA nanosheets. However, the cell viability significantly decreases for 4T1 cells incubated with PtCu-PEG-FA nanosheets and treated with 808 nm (1.0 W/cm^2) or 1064 nm (1.5 W/cm^2) laser for 10 min, which is attributable to hyperthermia due to the photothermal effect of PtCu-PEG-FA nanosheets to induce apoptosis of 4T1 cells. The confocal images (Fig. S13b in Supporting information) visually prove the photothermal killing effect towards 4T1 cells under 808 and 1064 nm lasers, respectively. Hemolysis experiments were carried out to evaluate the hemocompatibility of PtCu-PEG-FA nanosheets. It can be seen from Fig. S14 (Supporting information) that PtCu-PEG-FA nanosheets with different concentrations do not cause obvious hemolysis after incubation with erythrocytes, indicating the excellent hemocompatibility of PtCu-PEG-FA nanosheets for suitable *in vivo* biological applications.

Encouraged by the prominent photothermal and photoacoustic properties of PtCu nanosheets, we investigated the applications of PtCu-PEG-FA nanosheets for PAI-guided PTT *in vivo*. All animal-related procedures were ethically reviewed and approved by the Institutional Animal Care and Use Committees of Nanjing University of Posts and Telecommunications (IACUC-2022004). The laser fluences at mice's skin in our experiments were measured to be ~3.46 mJ pulse^{-1} cm^{-2} for 808 nm laser and ~2.09 mJ pulse^{-1} cm^{-2} for 1064 nm laser, which were lower than the international ANSI standard (<20 mJ pulse^{-1} cm^2), indicating that PtCu-PEG-FA nanosheets can be used for PAI-guided PTT *in vivo* by using both NIR-I and NIR-II lasers at the safe power density. As shown in Fig. 4a and Fig. S15 (Supporting information), clear photoacoustic signals derived from accumulation of PtCu-PEG-FA nanosheets in the site of 4T1 tumors can be observed after intravenous injection of PtCu-PEG-FA nanosheets for 36 h. After intravenous injection of PtCu-PEG-FA nanosheets for 72 h, the photoacoustic signal of PtCu-PEG-FA nanosheets disappears, indicating that PtCu-PEG-FA nanosheets have been almost completely cleared through metabolism at 72 h postinjection. It is suggested that PtCu-PEG-FA nanosheets can be efficiently enriched in the 4T1 tumor site through their permeability and retention effect, which are metabolizable. All these properties enable them to be a powerful candidate for PAI of 4T1 tumors.

PTT of 4T1 tumor-bearing mice by PtCu-PEG-FA nanosheets was then studied. As shown in Figs. 4b and c, the temperatures at the tumor sites of mice treated with PtCu-PEG-FA nanosheets increase to 53.5 and 49.8 °C under the irradiation of 808 and 1064 nm lasers for 4 min, respectively. In contrast, the temperatures at the tumor sites of mice injected with PBS only show an increase of less than 6 °C under laser irradiation. It is indicated that PtCu-PEG-FA nanosheets present good targeting and enrichment effect at the

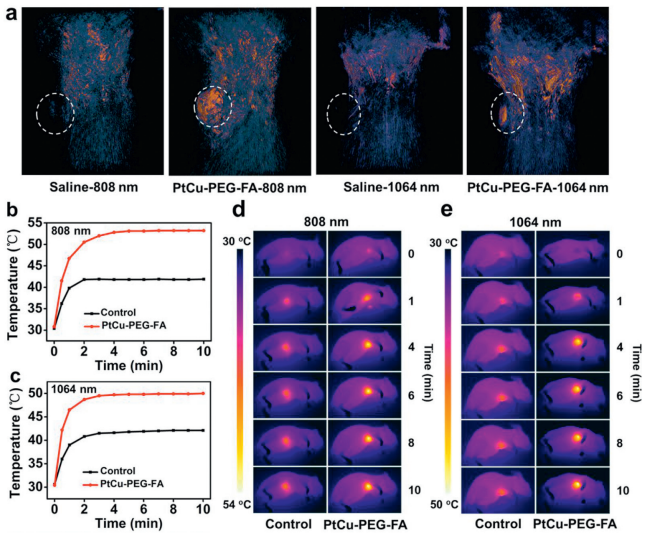

Fig. 4. (a) PAI of the whole body and tumor site under 808 or 1064 nm laser before and after intravenous injection of saline or PtCu-PEG-FA nanosheets. Photothermal heating curves of 4T1 tumors under (b) 808 or (c) 1064 nm laser after intravenous injection of PtCu-PEG-FA nanosheets or saline for 36 h. Photothermal imaging of 4T1 tumors under (d) 808 or (e) 1064 nm laser after intravenous injection of PtCu-PEG-FA nanosheets or saline for 36 h.

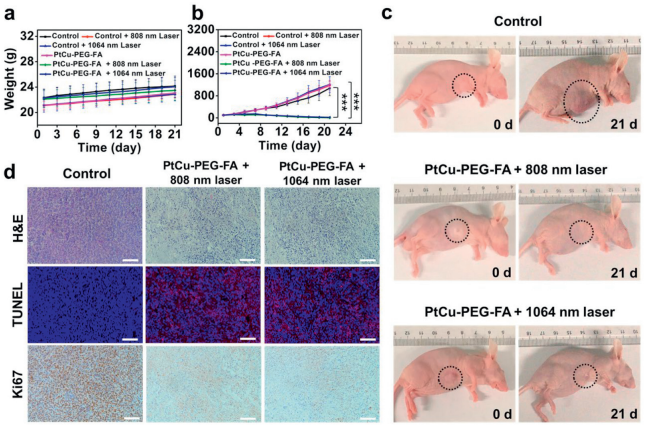

Fig. 5. (a) Body weights and (b) tumor volumes of the mice after various treatments. (c) Photographs of the mice before and after treatments. (d) H&E, TUNEL and Ki67 immunohistochemical staining images of tumor tissue slices. Scale bar: 500 μm. Data are presented as mean ± standard deviation (SD) ($n = 5$). $^{***}P < 0.001$.

4T1 tumor sites and show prominent photothermal heating performance in 4T1 tumors under 808 and 1064 nm lasers. Photothermal imaging of 4T1 tumors under 808 nm (Fig. 4d) and 1064 nm (Fig. 4e) lasers after intravenous injection of PtCu-PEG-FA nanosheets for 36 h further proves the highly efficient photothermal heating in 4T1 tumors. The enrichment of PtCu-PEG-FA nanosheets at the 4T1 tumor sites causes hyperthermia in a short time and leads to irreversible damages to cancer cells. What is more, the skin temperature of treated mice keeps a safe temperature zone (~43 °C), suggesting that the normal tissues are not destroyed under laser irradiation in the progress of PTT.

The body weights and tumor volumes were recorded to observe the PTT effect during 21 d. It can be seen from Fig. 5a that there is no significant difference for the body weights among different treatment groups in the course of PTT, indicating good biosafety of PtCu-PEG-FA nanosheets as PTT agents. The tumor volumes of mice without treatments by PtCu-PEG-FA nanosheets or NIR lasers consistently increase in the period of 21 d, while the tumor volumes of mice treated by both PtCu-PEG-FA nanosheets and NIR lasers give slight increase in the beginning of 6.5 d and then gradually shrink in the later of 14.5 d (Fig. 5b). The 4T1 tumors are almost eliminated and all mice survive after PTT for 21 d. Photographs of mice (Fig. 5c) and corresponding tumor volumes before and after different treatments (Fig. S16 in Supporting information) clearly present the PTT efficacy of PtCu-PEG-FA nanosheets under 808 and 1064 nm lasers. Hematoxylin-eosin (H&E) staining images of tumor tissue slices in the PtCu-PEG-FA+808 nm laser and PtCu-PEG-FA+1064 nm laser groups reveal apparent contractive tumor cell nucleus and loose tumor tissue structures, which are rarely seen in the control group (Fig. 5d). TdT-mediated dUTP Nick-End Labeling (TUNEL) staining images in the PtCu-PEG-FA+808 nm laser and PtCu-PEG-FA+1064 nm laser groups reveal a substantial number of apoptotic tumor cells (red fluorescence), but almost no apoptotic cells are found in the control group (Fig. 5d). Ki67 immunohistochemical staining images of tumor tissue slices demonstrate numerous positive cells (brown color) in the control group and very few positive cells in the PtCu-PEG-FA+808 nm laser and PtCu-PEG-FA+1064 nm laser groups (Fig. 5d). H&E, TUNEL and Ki67 immunohistochemical staining images of tumor tissue slices prove the effective NIR-II PTT by PtCu-PEG-FA nanosheets. Tumor inhibition in the process of 21-day treatment may be attributed to immunogenic cell death (ICD) induced by PtCu-PEG-FA-based PTT. According to relevant report [51] and our previous work [52], efficient PTT can induce ICD and then activate T cell-mediated immunity. Specifically, tumor cells can release damage-associated molecular patterns (DAMPs) including surface-exposed calreticulin (CRT), released high-mobility group protein B1 (HMGB1) and secreted adenosine triphosphate (ATP) in the process of ICD to induce migration and maturation of dendritic cells (DCs), which then activate antitumor immune response [51,52]. H&E staining images of major organs from the mice treated by PtCu-PEG-FA nanosheets and NIR lasers (Fig. S17 in Supporting information) confirm that PtCu-PEG-FA nanosheets have good biocompatibility and no side effect for PTT *in vivo* under NIR-I and NIR-II lasers. The biodistribution of PtCu-PEG-FA in major organs (heart, liver, spleen, lung and kidney) was measured by inductively coupled plasma-Mass Spectrometry (ICP-MS). As shown in Fig. S18 (Supporting information), there is very low amount of Pt and Cu elements in major organs, suggesting that PtCu-PEG-FA nanosheets can be metabolizable after PTT.

In summary, we have developed ultrasmall PtCu nanosheets as broadband NIR photothermal and photoacoustic agents. PtCu nanosheets show good photothermal effect with the PCEs of 20.4% under 808 nm laser and 32.7% under 1064 nm. The photoacoustic signal of PtCu nanosheets is strong and proportional to their concentrations. Functionalization of PtCu nanosheets with SH-PEG-FA endows them with good biocompatibility and 4T1 tumor-targeting function. Experiments *in vivo* demonstrate that 4T1 tumors in mice can be efficiently eliminated by the PAI-guided PTT of PtCu-PEG-FA nanosheets in both NIR-I and NIR-II biowindows without side effect and tumor metastasis. This kind of platinum-based 2D nanostructure enriches the library of broadband photothermal and photoacoustic agents in the NIR biowindow.

Declaration of competing interest

The authors declare that they have no known competing financial interests or personal relationships that could have appeared to influence the work reported in this paper.

CRediT authorship contribution statement

Ying Zhang: Writing – original draft, Project administration, Methodology, Investigation, Conceptualization. **Chuang Shen:** Software, Investigation, Formal analysis, Data curation. **Jiaxu Zhang:**

Investigation, Formal analysis, Data curation. **Qi Shen:** Methodology, Investigation, Formal analysis, Data curation. **Fei Xu:** Investigation, Data curation. **Shengheng Wang:** Methodology, Investigation. **Jiuyi Hu:** Formal analysis, Data curation. **Faisal Saleem:** Project administration, Conceptualization. **Feng Huang:** Supervision, Investigation, Conceptualization. **Zhimin Luo:** Writing – review & editing, Supervision, Project administration, Investigation, Conceptualization.

Acknowledgments

We acknowledge the National Natural Science Foundation of China (Nos. 22275096, W2432015), Natural Science Key Fund for Universities in Jiangsu Province (No. 22KJA430007), Qinglan Project of Jiangsu Province of China.

Supplementary materials

Supplementary material associated with this article can be found, in the online version, at doi:10.1016/j.cclet.2025.111059.

References

[1] Y. Liu, P. Bhattarai, Z. Dai, X. Chen, Chem. Soc. Rev. 48 (2019) 2053–2108.
[2] J. Hu, Y. Cheng, X. Zhang, Nanoscale 10 (2018) 22657–22672.
[3] D. Melo-Diogo, C. Pais-Silva, D.R. Dias, A.F. Moreira, I.J. Correia, Adv. Healthc. Mater. 6 (2017) 1700073.
[4] S. Mallidi, G.P. Luke, S. Emelianov, Trend. Biotechnol. 29 (2011) 213–221.
[5] J.W. Kim, E.I. Galanzha, E.V. Shashkov, H.M. Moon, V.P. Zharov, Nat. Nanotechnol. 4 (2009) 688–694.
[6] H. Moon, D. Kumar, H. Kim, et al., ACS Nano 9 (2015) 2711–2719.
[7] M.A. Patel, H. Yang, P.L. Chiu, et al., ACS Nano 7 (2013) 8147–8157.
[8] J.T. Robinson, S.M. Tabakman, Y. Liang, et al., J. Am. Chem. Soc. 133 (2011) 6825–6831.
[9] H. Tian, J. Lin, F. Zhu, et al., Chin. Chem. Lett. 34 (2023) 107577.
[10] J. Chen, C. Liu, D. Hu, et al., Adv. Funct. Mater. 26 (2016) 8715–8725.
[11] S.S. Chou, B. Kaehr, J. Kim, et al., Angew. Chem. Int. Ed. 125 (2013) 4254–4258.
[12] T. Liu, C. Wang, X. Gu, et al., Adv. Mater. 26 (2014) 3433–3440.
[13] S. Shen, Y. Chao, Z. Dong, et al., Adv. Funct. Mater. 27 (2017) 1700250.
[14] J. Shi, J. Li, Y. Wang, J. Cheng, C. Zhang, J. Mater. Chem. B 8 (2020) 5793–5807.
[15] C. Tan, L. Zhao, P. Yu, et al., Angew. Chem. Int. Ed. 129 (2017) 7950–7954.
[16] Z. Zhou, B. Li, C. Shen, et al., Small 6 (2020) 2004173.
[17] M.R.K. Ali, M.A. Rahman, Y. Wu, M.A. El-Sayed, Proc. Natl. Acad. Sci. U. S. A. 3 (2017) E3110–E3118.
[18] M. Chen, S. Tang, Z. Guo, et al., Adv. Mater. 26 (2014) 8210–8216.
[19] Y.S. Chen, W. Frey, S. Kim, et al., Nano Lett. 11 (2011) 348–354.
[20] P. Huang, J. Lin, W. Li, et al., Angew. Chem. Int. Ed. 125 (2013) 14208–14214.
[21] J.V. Jokerst, A.J. Cole, D.V. Sompel, S.S. Gambhir, ACS Nano 6 (2012) 10366–10377.
[22] J.V. Jokerst, M. Thangaraj, P.J. Kempen, R. Sinclair, S.S. Gambhir, ACS Nano 6 (2012) 5920–5930.
[23] C. Kim, E.C. Cho, J. Chen, et al., ACS Nano 4 (2010) 4559–4564.
[24] S. Tang, M. Chen, N. Zheng, Small 10 (2014) 3139–3144.
[25] Y. Wu, M.R.K. Ali, B. Dong, et al., ACS Nano 12 (2018) 9279–9290.
[26] Z. Zhou, X. Wang, H. Zhang, et al., Small 17 (2021) 2007486.
[27] Z. Zhou, Y. Wang, F. Peng, et al., Angew. Chem. Int. Ed. 61 (2022) e202115939.
[28] B. Xue, X. Geng, H. Cui, et al., Chin. Chem. Lett. 34 (2023) 108140.
[29] K. Zhang, X. Meng, Y. Cao, et al., Adv. Funct. Mater. 28 (2018) 1804634.
[30] M. Rycenga, Z. Wang, E. Gordon, et al., Angew. Chem. Int. Ed. 48 (2009) 9924–9927.
[31] A.M. Gobin, M.H. Lee, N.J. Halas, et al., Nano Lett. 7 (2007) 1929–1934.
[32] Z. Deng, C. Jiang, M.R. Younis, et al., Chin. Chem. Lett. 32 (2021) 2411–2414.
[33] S. Li, Z. Li, Q. Hao, et al., Chin. Chem. Lett. 35 (2024) 108636.
[34] K.A. Homan, M. Souza, R. Truby, et al., ACS Nano 6 (2012) 641–650.
[35] X. Huang, S. Tang, B. Liu, B. Ren, N. Zheng, Adv. Mater. 23 (2011) 3420–3425.
[36] X. Huang, S. Tang, X. Mu, et al., Nat. Nanotechnol. 6 (2011) 28–32.
[37] A. Dumas, P. Couvreur, Chem. Sci. 6 (2015) 2153–2157.
[38] Q. Wang, H. Wang, Y. Yang, et al., Adv. Mater. 31 (2019) 1904836.
[39] F. Saleem, Z. Zhang, B. Xu, et al., J. Am. Chem. Soc. 135 (2013) 18304–18307.
[40] Z. Zhang, Z. Luo, B. Chen, et al., Adv. Mater. 28 (2016) 8712–8717.
[41] W. Zuo, N. Liu, Z. Chang, et al., Chem. Eng. J. 442 (2022) 136125.
[42] J. Ouyang, C. Feng, X. Ji, et al., Angew. Chem. Int. Ed. 131 (2019) 13539–13544.
[43] X. Yang, M. Yang, B. Pang, M. Vara, Y. Xia, Chem. Rev. 115 (2015) 10410–10488.
[44] M. Yin, J. Tong, F. Meng, et al., ACS Appl. Mater. Interfaces 14 (2022) 49471–49482.
[45] L. Song, J. Li, Small 11 (2024) 2407787.
[46] Z. Wu, W. Li, C. Luo, et al., Adv. Funct. Mater. 25 (2015) 6527–6537.
[47] M. Manikandan, N. Hasan, H. Wu, Biomaterials 34 (2013) 5833–5842.
[48] M.K. Off, A.E. Steindal, A.C. Porojnicu, et al., J. Photoch. Photobiol. B 80 (2005) 47–55.
[49] L. Li, W. Wang, Y. Chai, et al., Adv. Funct. Mater. 27 (2017) 1701011.
[50] Y. Wu, C. Liu, C. Wang, et al., Nat. Commun. 12 (2021) 3881.
[51] J. Li, L. Xie, B. Li, et al., Adv. Mater. 33 (2021) 2008481.
[52] Z. Huang, J. Song, S. Huang, et al., Nano Lett. 24 (2024) 7764–7773.